metals

MDPI

Article

Solid-State Additive Deposition of AA7075 on AZ31B Substrate: Heat Treatment to Improve the Corrosion Fatigue Resistance

Sugrib Kumar Shaha [1,*], Dyuti Sarker [1] and Hamid Jahed [2]

[1] School of Materials Science and Engineering, Georgia Institute of Technology, 771 Ferst Drive NW, Atlanta, GA 30332, USA
[2] Department of Mechanical & Mechatronics Engineering, University of Waterloo, 200 University Ave W, Waterloo, ON N2L 3G1, Canada
* Correspondence: sshaha@gatech.edu

Abstract: The influence of heat treatment on the coating microstructure, nanomechanical, and corrosion fatigue properties of solid-state deposition of AA7075 aluminum alloy on AZ31B cast Mg alloy is studied in detail. Transmission electron microscopy (TEM) microstructural analysis shows columnar grain at the interface of AA7075/AZ31B. Electron backscatter diffraction (EBSD) observation discovered elongated grains with a high fraction of deformed grain boundaries as-deposited and heat-treated at 200 °C conditions. In contrast, the annealed samples show recrystallized grains with increasing temperatures from 200 °C to 400 °C. The residual stress of the coating at the surface and subsurface measured by X-ray diffraction shows −55 MPa and −122 MPa, respectively, which transferred to tensile with increasing the annealing temperature up to 400 °C. Annealing treatment of the AA7075 coating considerably improved the nanomechanical properties and corrosion fatigue resistance. With increasing the annealing temperature from 200 °C to 400 °C, the hardness of the coating decreased, while the modulus increased significantly. The analysis of fatigue fracture surfaces revealed that corrosive solution entered through the cracks and accelerated the crack propagation, lowering the fatigue life. However, the presence of recrystallized grains improved the corrosion fatigue resistance.

Keywords: corrosion fatigue; solid-state additive; AA7075; AZ31B; recrystallization

Citation: Shaha, S.K.; Sarker, D.; Jahed, H. Solid-State Additive Deposition of AA7075 on AZ31B Substrate: Heat Treatment to Improve the Corrosion Fatigue Resistance. *Metals* **2022**, *12*, 1578. https://doi.org/10.3390/met12101578

Academic Editor: Changdong Gu

Received: 5 August 2022
Accepted: 17 September 2022
Published: 23 September 2022

1. Introduction

Mg is one of the lightest metallic materials, the potential candidate for light-weighting. The resistance to wear and corrosion of Mg alloys should be improved to extend the application of Mg alloys for structural applications, and surface modification is one of them [1–6]. The typical surface modification processes [7–10] of the Mg alloys are conversion coating, laser processing, physical vapor deposition, micro-arc oxidation, and solid-state additive deposition, namely cold spray (CS) deposition, etc. Among them, the CS process is the most effective and better for coating all materials [5,6]. In this process, the formed protective coatings improve the wear and corrosion resistance of different materials, including metals and ceramics. Rokni et al. [11,12] deposited AA7075 alloy on a wrought AA7075 plate using a high-pressure cold spray system. Agar et al. [13] improved the corrosion resistance of the aluminum alloys AA2024 and AA7075 deposited in the CS system. The CS deposited AA7075 shows better corrosion and wear resistance [14,15]. The composite coating also can be deposited in the CS process. Spencer et al. [16] deposited Al-Al_2O_3 particle-reinforced composite coatings on AZ91E substrates. Omar et al. [17] also deposited ceramic materials TiO_2 on the pure-Cu and AA1050 alloy in the CS process and discussed the bonding mechanism. Our recent studies [18–20] confirmed that the fatigue and corrosion fatigue resistance of the AZ31B Mg alloy considerably improved by developing a coating layer of high-strength AA7075 alloy. The presence of lower coating defects and compressive residual stress improved the fatigue performance. However, the fatigue fracture surface

revealed that coatings were delaminated from the interface leading to the final fracture. So, the dissimilar coating/substrate performance predominantly depends on the strong interfacial bonding between coating and substrate [21]. The interfacial bonding can be improved by optimizing the process parameters [22] or the post-processing, such as plasma electrolytic oxidation (PEO) [23], shot-peening [24], heat treatment [25], etc.

Mangalarapu et al. [26] investigated the microstructure and mechanical properties of the Al-6061 alloy CS coatings in as-deposited and heat-treated conditions. They concluded that heat treatment improved the bonding strength of the CS coating. Spencer and Zhang [27] improved the corrosion resistance of AZ91 Mg substrates by depositing pure Al in the CS process followed by annealing at 400 °C, which yields different types of intermetallic layers, including Mg_2Al_3 and $Mg_{17}Al_{12}$ at the coating/substrate interface [28]. Zhang et al. [29] also examined the nanomechanical behavior of post-processed CS coating to understand the effect of annealing the intermetallic layers. They reported no significant differences in nanomechanical properties between Mg_2Al_3 and $Mg_{17}Al_{12}$ intermetallics [30]. At the same time, the microhardness of the pure Mg substrate was substantially lower than the intermetallics [31]. Such intermetallic layers can effectively improve the resistance to corrosion of the Mg and its alloys. At the same time, they also possess an anodic barrier that enhances corrosion resistance [32,33]. The intermetallics have higher hardness than the substrate, so they effectively increase the wear resistance. Our recent study [34] confirmed that heat treatment changed the interfacial microstructure by forming several types of intermetallics of $Mg_{17}Al_{12}$ and Mg_2Al_3 at the coating/substrate interface, which enhanced the bonding strength and led to better tensile properties of the coated materials. So, it is essential to investigate a thorough microstructural analysis to achieve the optimum mechanical properties, specifically the corrosion fatigue resistance. However, to the best of the authors' knowledge, there was no study on the effect of heat treatment on the solid-state deposited microstructure and corrosion fatigue resistance of CS AA7075 alloy on the Mg substrate.

Therefore, in the present study, the TEM, EBSD, and XRD analyses were performed to understand the effect of heat treatment on the residual stress and grain growth mechanism in the coating. Finally, the nanoindentation and corrosion fatigue tests were conducted to understand the performance of the CS AA7075 alloy on the Mg substrate.

2. Experimental

This study used commercially available cast AZ31B Mg alloy as a substrate material. The CS coating was prepared from gas atomized AA7075 powder. The distribution of the powder can be found in [18]. The powder was deposited on the flat coupon for microstructural analysis and dog-bone shape tensile samples for corrosion fatigue testing. The details of the coating process parameters are described elsewhere in [18]. After fabrication, the coated samples experienced heat treatment in the sand bath furnace at three different temperatures of 200 °C, 300 °C, and 400 °C for one hour. The heat-treated samples were water quenched to retain the microstructure. The post-processed coating was polished following the standard metallographic technique. After mechanical polishing, specimens were vibratory polished in colloidal SiO_2 for 2 h for Electron Backscatter Diffraction (EBSD) analysis. EBSD data were acquired in the FE-SEM with a fully automatic Oxford SD detector operated by AZtecHKL Technology. The EBSD process parameters were considered operating voltage, working distance, and tilt angle of 20 kV, 15 mm, and 70°, respectively. The obtained data were analyzed using the Aztec crystal software.

The microstructural analysis was performed on the FIB lift out (<100 nm) using transmission electron microscopy (TEM), JEOL-2010F, equipped with energy-dispersive X-ray spectroscopy (EDX). The operating voltage of 200 keV was set to obtain bright field (BF) images.

The residual stress (RS) was measured at the surface and subsurface (100 µm depth) using a Bruker D8-Discover equipped with a VÅNTEC-500 area detector and Cu-Kα radiation at a voltage of 40 kV and current of 40 mA. The RS measurement was conducted using the $Sin^2\Psi$ method at a constant 2θ angle between the incident beam and detector.

Nanoindentation was performed using a Micro-Material's Nano Test Platform 3 and an indenter size of 100 nm. The test was performed at a constant loading rate of 500 μN/s up to a maximum load of 30 mN. At least five indents were made to calculate the hardness and reduced elastic modulus Er. Then, the elastic modulus E was calculated from Er for each heat-treated condition. The hardness and nanoindentation calculation was explained in [35].

Based on the tensile tests [34], corrosion fatigue tests were conducted for as-deposited (AD) and heat-treated 300 °C conditions. The fatigue tests were performed using an Instron RR Moore four-point rotating-bending fatigue testing machine (Norwood, MA, USA) in a fully reversed ($R = -1$) load-controlled condition. The tests were conducted at a fixed stress amplitude of 100 MPa and a frequency of 30 Hz. Corrosion fatigue tests were conducted in the customized chamber where 3.5% NaCl solution was used as an electrolyte. At least two samples were tested in each condition. Detailed fatigue setup can be seen in [18]. In addition, fracture surfaces were investigated using Field Emission Scanning Electron Microscopy(FE-SEM) equipped with EDX.

3. Results and Discussion

3.1. Microstructure Evolution and Residual Stress

Figure 1a shows the cross-sectional TEM bright field image and corresponding EDX line scan. The image shows their distinct regions; substrate (AZ31B), interface, and AA7075 coating in AD conditions. As noticed in Figure 1a, the EDX line scan at the interface of the substrate/coating in AD condition displays a mixture of Mg/Al with a 200–300 nm thickness of intermetallics $Mg_{17}Al_{12}$. Columnar grains were noticed just adjacent to the interface, while equiaxed grains were identified in the substrate. In contrast, as specified by the red arrows in the BF image (Figure 1b), elongated grains with high dislocation density and $MgZn_2$ precipitates (blue arrows) at the grain boundaries of the HAADF-STEM images (Figure 1c) are detected in CS AA7075 coating. During the CS process, the coating particles strike the substrate and deform severely, which induces a high density of dislocations. The dislocation density is so high that it can not be differentiated, as seen in black spots in the coating microstructure. It should be mentioned that the coating particles were traveling at a very high velocity (supersonic speed) when they hit the substrate; the momentum becomes zero in a very short time (nanosecond) that converts high energy results adiabatic share deformation leading to the formation of the coating. A very dense coating is formed due to a high energy conversion rate. As seen in Figure 1a, there were no defects noticed at the interface or in the coating layer in the AD. At the same time, no hairline cracks were discovered at the interface of the coating/substrate in the AD condition. This implies that the coating was very dense and defects-free, resulting in better performance with these types of deposition. A detailed analysis of the interfacial microstructure is presented in our previous work [36].

To understand the recrystallization behavior of the CS AA7075 coating, EBSD analysis was performed in different experimental conditions: as-deposited and heat-treated at 200 °C, 300 °C, and 400 °C. Figure 2 shows maps of the inverse pole figure of the AD and heat-treated coating. Similar types of elongated grains identified in TEM micrographs (Figure 1b) in AD conditions were noticed in the inverse pole figure map in Figure 2a. The grain morphology in the sample heat-treated at 200 °C (Figure 2b) was about the same in AD microstructure. However, increasing the annealing temperature from 200 °C to 300 °C, some of the elongated grains were transformed to equiaxed, as seen in Figure 2c. The grains are further recrystallized and transformed to fully equiaxed at the sample heat-treated to 400 °C (Figure 2d).

The grain boundaries of the CS AA7075 were divided into three categories: deformed grains (up to 5°), sub-structure (5 to 15°), and recrystallized grains (15° and above). The qualitative analysis of the CS AA7075 is presented in Figure 3. The fraction of different types of grains vs. heat treatment temperatures are plotted in Figure 3. No recrystallized grains were identified in AD conditions. At the same time, a fraction of 88.5% deformed grains and 11.5% substructures were noticed in AD conditions. In contrast, the fraction of recrystallized

grains increased to ~99%while the fraction of deformed and sub-grains decreased to almost zero at the heat treatment temperatures of 400 °C. About 50% recrystallized and substructures in each type of grains were noticed in the sample heat-treated at 300 °C. At the same time, the deformed grains are about 5%. It is worth mentioning that deformed grains were transformed into sub-grains at 200 °C. However, there were no recrystallized grains at that temperature as well. As the temperature was well below the recrystallization of the AA7075 alloy, a significant recovery occurred at 200 °C temperature. In contrast, when the temperature reached above the recrystallization temperature, i.e., 300 °C, most deformed grains transformed to sub-grains, followed by recrystallized grains. This was in agreement with the previous studies regarding post-processing, such as annealing of pure Al coating on the Mg substrates [27,29].

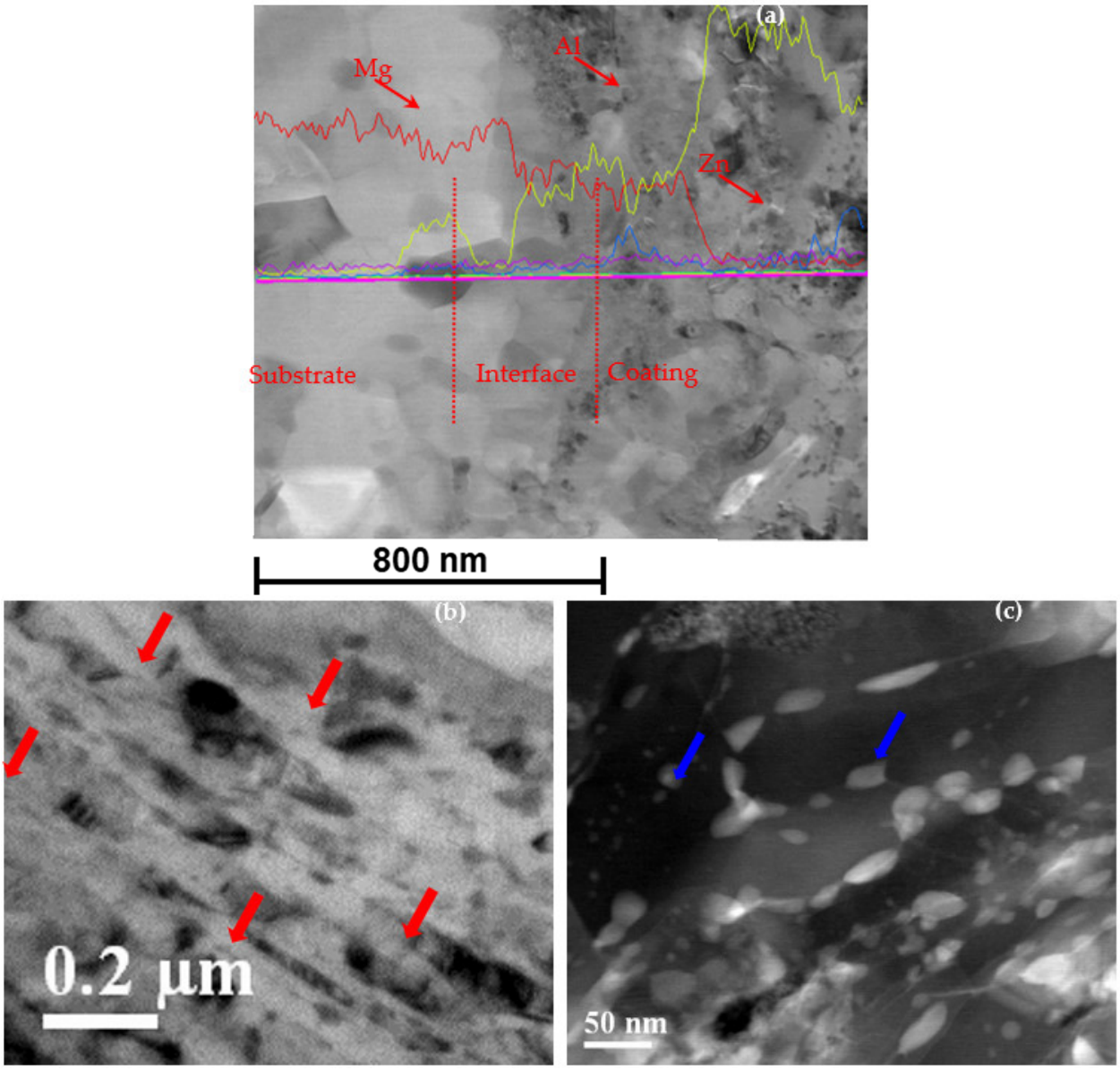

Figure 1. Typical bright field TEM images with EDX line scan show (**a**) the interface microstructure of AA7075 cold spray coating on AZ31B substrate, (**b**) bright field (BF), and (**c**) high-angle annular dark-field scanning transmission (HAADF-STEM) electron image taken at [110] zone axis coating show the elongated grains. Note: Red and blue arrows indicate the highly dense dislocation area and MgZn2 intermetallics, respectively.

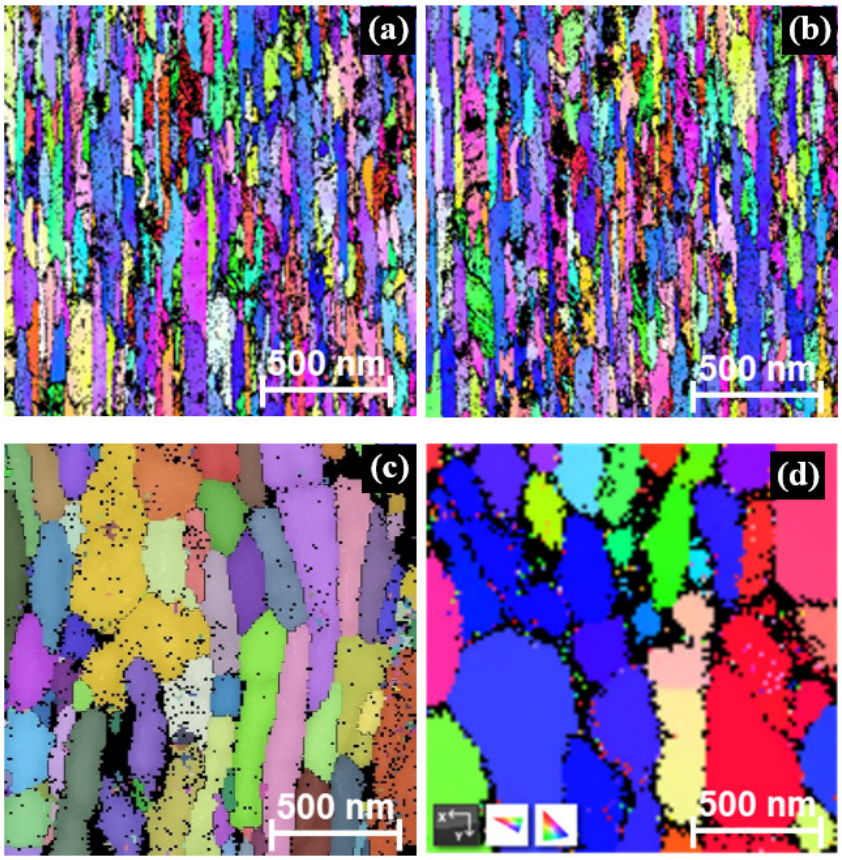

Figure 2. The IPF maps of the cold spray deposited coating show elongated and deformed grains in (**a**) as-deposited conditions, while recrystallized grains are identified in heat-treated at (**b**) 200 °C, (**c**) 300 °C, and (**d**) 400 °C conditions.

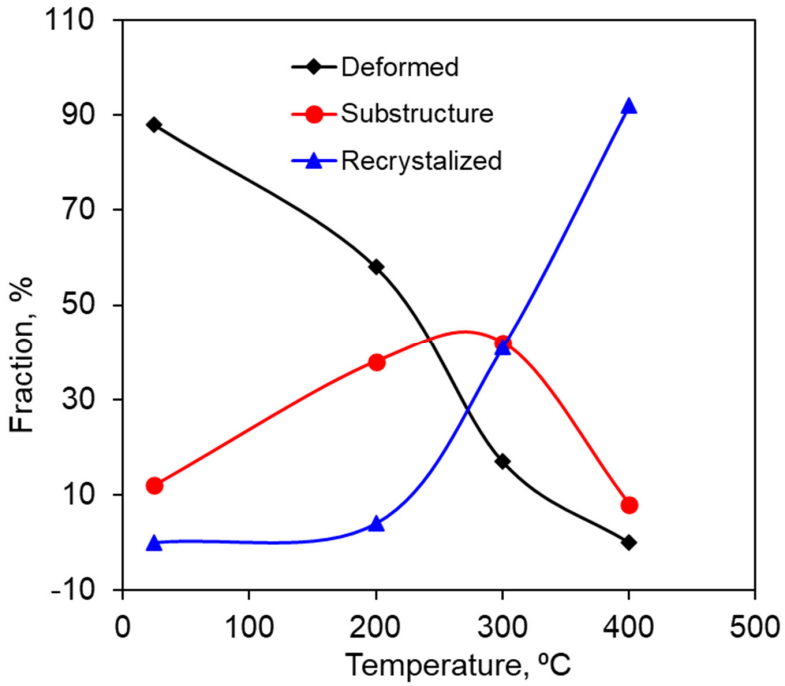

Figure 3. Effect of the annealing temperature on the fraction of different types of grains of the AA7075 coating deposited on the AZ31B Mg alloy in the cold spray process.

It is well established that the recovery and recrystallization of metals and alloys are diffusion controlled, which influences by temperature [37,38]. Wang et al. [37] reported the recrystallization behavior of cold-rolled AA7075 alloy sheets. They found that recovery occurred during any heating rate, even at the fast heating rate. The recovery and recrystallization consume the stored energy and change the grain morphologies. At the same time, the recovery reduces dislocation density, decreasing the stored energy and resulting in a lower number of potential nucleation sites for recrystallization. At lower temperatures, recovery was dominant, resulting in less recrystallization. However, increasing the temperature, the diffusion rate increased significantly, accelerating the recrystallization.

The measured residual stress of the CS AA7075 coating on AZ31B Mg alloy substrate is depicted in Figure 4. The surface and subsurface (~100 µm) of the coating in AD conditions achieved an average compressive residual stress of −52 MPa and −120 MPa. This implies that a residual stress relaxation occurred at the surface of the CS coating. Ghelichi et al. [39] reported similar behavior in residual stress of the CS coating of AA7075 on the AA5052 substrate. Two mechanisms, (i) the temperature gradient and (ii) thermal conductivity, can be attributed to the development of residual stress in the cold spray process [40]. When the hot coating material strikes the cold substrate, it rapidly cooldown and forms the coating. As the material is heated by carrier gas, it is expanded during heating. Hence, a compressive force normal to the substrate exerted on the coating results in bulging the coating upward, which is restricted by surrounding cold materials. At high-temperature strength of the materials decreases and yields easily. During the heating process, the material experiences thermal expansion, yielding the materials, leading to the thermal strain to plastic strain. As the thermal strain was converted to plastic strain during heating, additional strain is required to compensate during the cooling. The high velocity of the particles and cyclic transformation of the strain caused a high magnitude residual stress in the coating.

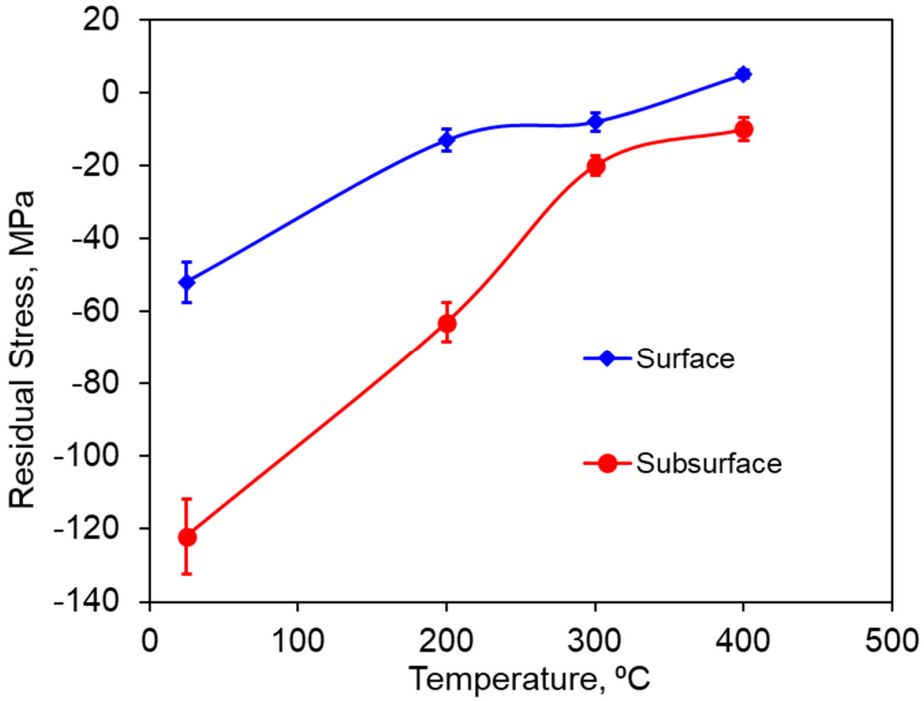

Figure 4. Residual stress distribution in the coating surface and subsurface measured by XRD showing compressive to tensile residual stress due to heat treatment.

At the same time, the differential thermal conductivity also contributes to the residual stress. The common feature of the CS process is adiabatic share deformation. In this process, the deposited layer deformed heavily and dissipated heat through the substrate. As the substrate and coating materials are dissimilar, there would be a gradient in heat flow. As

the thermal conductivity of the AZ31B Mg alloys is lower than the AA7075, heat will be dissipated faster in the substrate during the CS process. Thus, compressive residual stress will be developed in the coating [16,41].

As seen in Figure 4, the compressive residual stress relaxed with increasing heat treatment, leading to tensile residual stress up to 5 MPa at the surface of the sample heat-treated at 400 °C. As discussed earlier (Figure 3), the recovery of the dislocations and recrystallization followed by water quenching is responsible for the change of compressive to tensile residual stress at the surfaces. In contrast, the residual stress at the subsurface is still compressive. As the subsurface developed very high compressive residual stress, which worked as a driving force for recrystallization, faster recovery and recrystallization led to the sharp reduction of the residual stress. However, the remaining compressive residual stress at the subsurface was developed to compensate for the tensile residual stress formed at the surface during quenching. It is worth mentioning that compressive residual stress remains in the sample heat-treated at 300 °C (Figure 4), indicating partial recovery or recrystallization of the coating.

3.2. Nanomechanical Properties

Figure 5a demonstrates the typical nanoindentation load–displacement (P-d) curves obtained from the AA7075 CS coating at different conditions AD and heat-treated at 200 °C, 300 °C, and 400 °C. The nano-hardness (nHV) and reduced elastic modulus (Er) were determined from the load–displacement curves and plotted with the different temperatures. The average value of Er of the CS AA7075 coating in AD condition is ~72 GPa, and the elastic modulus (E) value was ~68 GPa. This indicated that the Er measure by the nanoindentation delivers a reliable procedure to obtain the elastic property. The hardness and elastic modulus of the CS coating obtained in nanoindentation are comparable to the bulk AA7075 aluminum alloys [41]. As seen in Figure 5b, the obtained Er in two heat-treated conditions at 300 °C and 400 °C were the same value of ~83 GPa, which are significantly higher than the CS AA7075 coating (72 GPa) in the AD condition. The P-d curves shown in Figure 5a demonstrate the significantly higher penetration depth in the sample heat-treated at 400 °C compared to the AD AA7075 coating, corresponding to the lower hardness.

The sample heat-treated at 300 °C and 400 °C obtained lower nano-hardness (nHV) values of 1.89 GPa and 1.73 GPa, respectively. However, the nHV values are substantially higher than those of the AD (2.13 GPa) and heat-treated at 200 °C (1.98 GPa) CS AA7075 coating. As seen in Figure 1, a high density of dislocations and deformed grains are responsible for higher hardness and lower modulus of elasticity. At the same time, the dislocations recovery (as depicted in Figure 3) and relaxation of residual stress (as illustrated in Figure 4) of the heat-treated samples decreased the hardness and increased the modulus of elasticity.

3.3. Corrosion Fatigue

Based on the tensile properties presented in [34], corrosion fatigue tests were conducted on the AD and 300 °C heat-treated conditions. Figure 6 illustrates the comparison of the AD and 300 °C heat-treated samples tested in 3.5% NaCl solution at a stress amplitude of 100 MPa. The obtained results of the corrosion fatigue tests revealed the efficiency of heat treatment of the CS coatings in protecting AZ31B from the corrosive environment. Generally, the heat-treated samples displayed excellent corrosion fatigue resistance compared to the AD condition. The fatigue life of heat-treated at 300 °C samples increased substantially in the 3.5% NaCl environment. The range of fatigue life of the CS AA7075 coating in AD conditions was between 3.5×10^4 and 17×10^4 cycles while the sample heat-treated at 300 °C exhibited better fatigue life between 19.5×10^4 and 24.4×10^4 cycles. As seen in Figure 6, the CS specimen showed lower fatigue performance in the corrosive environment. This can be attributed to the lower corrosion properties of AA7075 alloy in highly deformed conditions. At the same time, the improvement of fatigue life in the sample heat-treated at 300 °C can be associated with the microstructure in Figure 2. As

discussed in [34], heat treatment increased the tensile strength of the CS AA7075 coating on the AZ31B Mg alloy, which enhances the fatigue life in a similar testing condition.

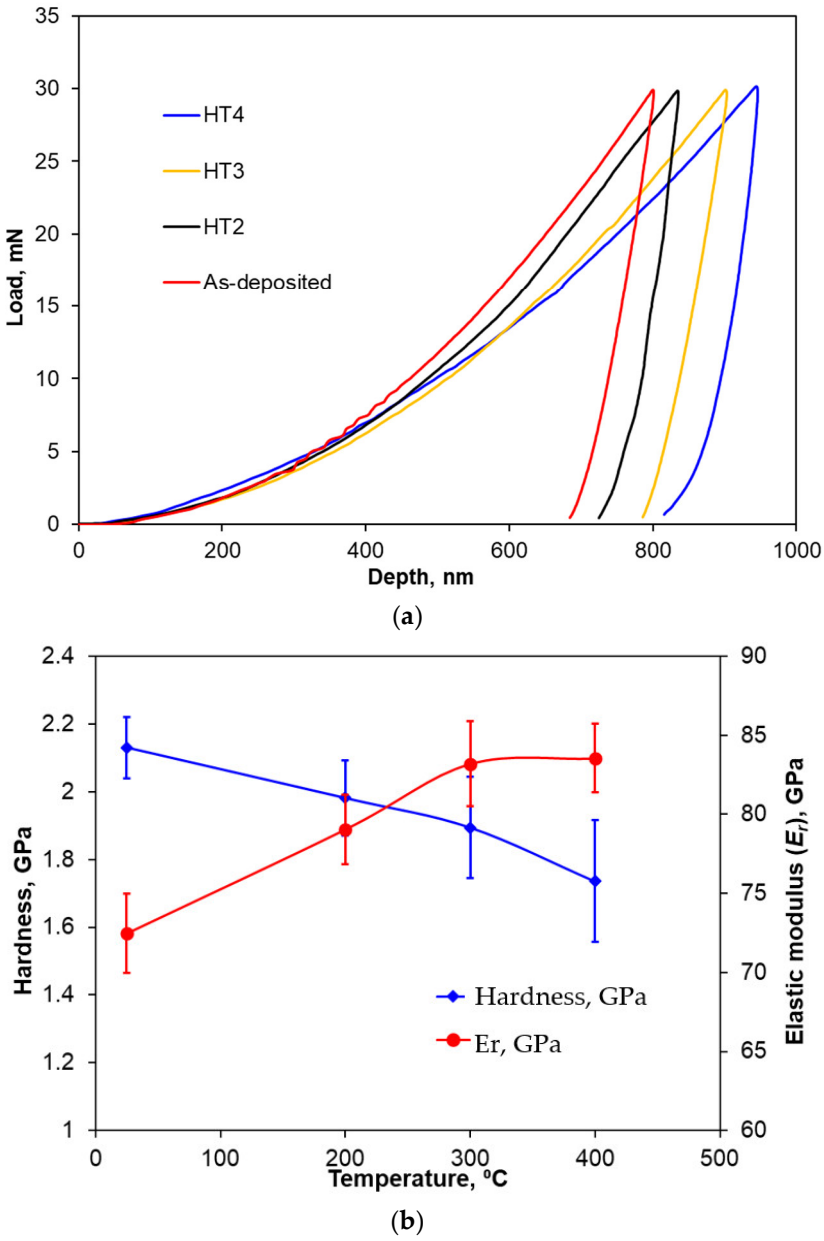

Figure 5. (**a**) The load–displacement curves and (**b**) the hardness and modulus of the as-deposited and heat-treated AA7075 coating obtained via nanoindentation tests.

Figure 7 portrays the corrosion fatigue fracture surfaces of AD and 300 °C heat-treated samples tested at a stress amplitude of 100 MPa. Both samples show similar types of fracture behavior during testing. No debonding identified in both cases indicates strong interfacial bonding between coating and substrate. The fatigue fracture surface shows large corrosion pits (red arrows in Figure 7) with visible cracks in the coating. At the same time, localized cavities (blue arrow in Figure 7) and hairline cracks were identified on the fracture surfaces, allowing the NaCl solution to enter and react with the substrate's interface. Those pits grow over time and transform into a large cavity, potential sites for the stress concentration caused by the initiation of cracks. Multiple cracks originating from concave surface corrosion pits advancing along the final fracture zone were observed (Figure 7). The corrosion products, including the oxides and hydroxides, are displayed on both fracture surfaces. A detailed analysis of the corrosion products can be seen in [20].

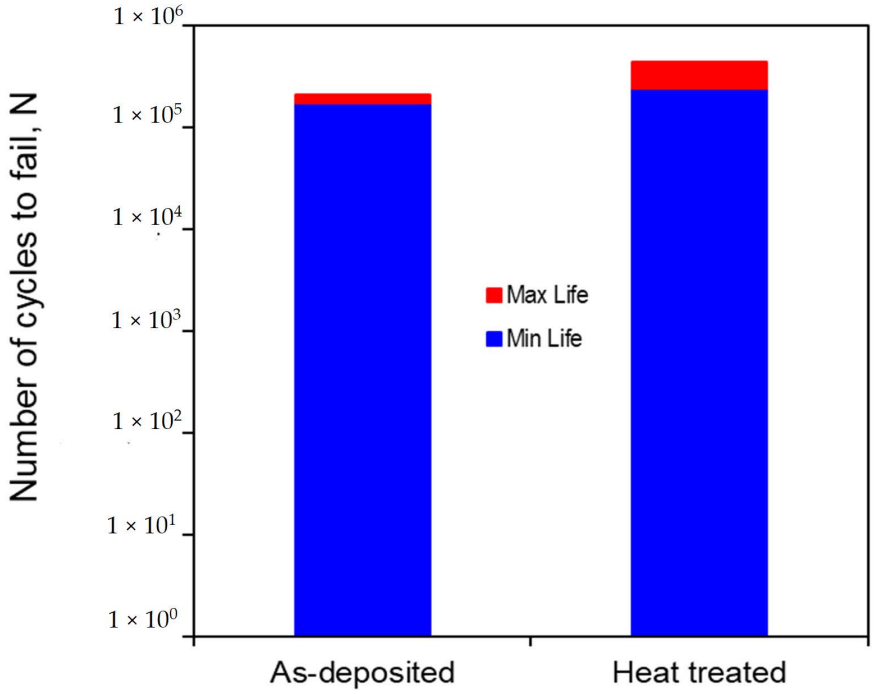

Figure 6. A comparison of the corrosion fatigue life between as-deposited and heat-treated at 300 °C of the AA7075 cold spray coated AZ31b Mg alloy.

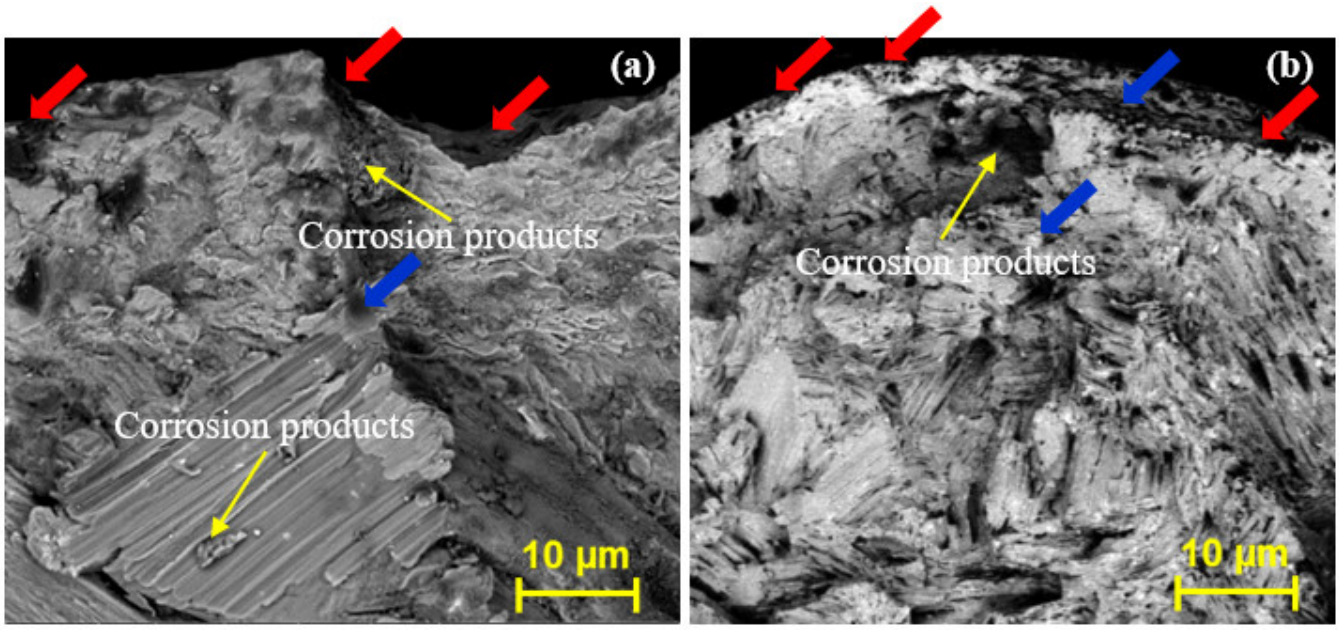

Figure 7. Fatigue fracture surfaces show the crack initiation and propagation in the (**a**) as-deposited and (**b**) heat-treated at 300 °C of the AA7075 cold spray coated AZ31b Mg alloy. Note: Red and blue arrows indicated the cossorion pits at the outer surfaces and on the fracture surface, rescectively.

Higher corrosion resistance and more extended fatigue performance are always desirable in a coating that protects Mg alloys. Therefore, finding out the main reason that controls the corrosion fatigue performance of the coatings can be helpful to the extent of the application of Mg alloys. Usually, defects such as pores, chemistry, and coating microstructures generally influence corrosion fatigue performance. In the corrosion fatigue test, micro-cracks and pits are the common sites for nucleating and initiating the fatigue cracks. Those enable the nucleation and propagation of cracks leading to premature failure,

resulting in short fatigue life. However, due to the presence of compressive residual stress in CS AA7075 coating, the fatigue crack initiation was effectively slower by closing the micro-cracks resulting in longer fatigue life. However, intermetallics in the AA7075 CS coatings (as seen in Figure 1) formed localized galvanic cells around them, forming the pits and potential sites for crack initiation. Hence, the effect of compressive residual stress is faded in the corrosive environment. In contrast, heat treatment at 300 °C dissolved the intermetallics, potentially reducing the crack initiation sites, resulting in longer fatigue life.

4. Conclusions

The effect of heat treatment on the corrosion fatigue performance of a CS AA7075 coating on AZ31B in a 3.5% NaCl solution at room temperature was studied. Based on the obtained results analysis above, the following conclusions can be made:

- TEM and EBSD microstructural analysis identified elongated grains with a high dislocation density observed in the AA7075 coating.
- The quantitative EBSD analysis shows above 90% highly deformed grains. In contrast, fully recrystallized grains were identified in the sample heat-treated at 400 °C temperature, while ~50% recrystallized and deformed grains were noticed in the sample heat-treated at 300 °C temperature.
- A maximum compressive residual stress of −52 MPa and −120 MPa was measured at the surface and subsurface in as-deposited conditions. In contrast, a tensile residual stress of 5 MPa was measured on the surface of the sample heat-treated at 400 °C temperature.
- During heat treatment, a decreasing trend in hardness and an increasing trend in elastic modulus was noticed in the CS AA7075 coating.
- A significant improvement in corrosion fatigue life of the CS AA7075 followed by heat treatment at 300 °C temperature was achieved. This can be recognized due to recrystallization and recovery of the grain structure.

Author Contributions: Conceptualization, S.K.S. and D.S.; methodology, S.K.S.; software, D.S.; validation, S.K.S., H.J. and D.S.; formal analysis, S.K.S. and D.S.; investigation, S.K.S.; resources, S.K.S.; data curation, S.K.S.; writing—original draft preparation, D.S.; writing—review and editing, S.K.S. and H.J.; visualization, S.K.S.; supervision, H.J.; project administration, H.J.; funding acquisition, H.J. All authors have read and agreed to the published version of the manuscript.

Funding: The authors would like to gratefully acknowledge the financial support of the Natural Sciences and Engineering Research Council (NSERC) of Canada under Discovery grant RGPIN 312053, Automotive Partnership Canada (APC) program under APCPJ 459269-13 grant, and Research Tools and Instruments (RTI) program under EQPEQ 458441-2014 grant.

Institutional Review Board Statement: Not applicable.

Informed Consent Statement: Not applicable.

Data Availability Statement: The data presented in this study are available on request from the corresponding author.

Conflicts of Interest: The authors declare no conflict of interest.

References

1. Ahmed, U.; Yi, L.; Fei, L.F.; Yasir, M.; Li, C.-J.; Li, C.-X. Enhancement of Corrosion Resistance and Tribological Properties of LA43M Mg Alloy by Cold-Sprayed Aluminum Coatings Reinforced with Alumina and Carbon Nanotubes. *J. Therm. Spray Technol.* **2021**, *30*, 668–679. [CrossRef]
2. Wan, S.; Cui, X.; Jin, Q.; Ma, J.; Wen, X.; Su, W.; Zhang, X.; Jin, G.; Tian, H. Microstructure and properties of cold sprayed aluminum bronze coating on MBLS10A-200 magnesium-lithium alloy. *Mater. Chem. Phys.* **2022**, *281*, 125832. [CrossRef]
3. Chakradhar, R.P.S.; Mouli, G.C.; Barshilia, H.; Srivastava, M. Improved Corrosion Protection of Magnesium Alloys AZ31B and AZ91 by Cold-Sprayed Aluminum Coatings. *J. Therm. Spray Technol.* **2021**, *30*, 371–384. [CrossRef]
4. Akisin, C.J.; Venturi, F.; Bai, M.; Bennett, C.J.; Hussain, T. Microstructure, mechanical and wear resistance properties of low-pressure cold-sprayed Al-7 Mg/Al2O3 and Al-10 Mg/Al2O3 composite coatings. *Emergent Mater.* **2021**, *4*, 1569–1581. [CrossRef]

5. Sabard, A.; McNutt, P.; Begg, H.; Hussain, T. Cold spray deposition of solution heat treated, artificially aged and naturally aged Al 7075 powder. *Surf. Coat. Technol.* **2020**, *385*, 125367. [CrossRef]
6. Tsaknopoulos, K.; Sousa, B.; Massar, C.; Grubbs, J.; Siopis, M.; Cote, D. A Through-Process Experimental Approach to Enable Optimization of Cold Sprayed Al 7075 Consolidation Performance. *JOM* **2022**, *74*, 249–259. [CrossRef]
7. Zhu, L.; Song, G. Improved corrosion resistance of AZ91D magnesium alloy by an aluminium-alloyed coating. *Surf. Coat. Technol.* **2006**, *200*, 2834–2840. [CrossRef]
8. Zhang, M.-X.; Kelly, P.M. Surface alloying of AZ91D alloy by diffusion coating. *J. Mater. Res.* **2002**, *17*, 2477–2479. [CrossRef]
9. Zhang, M.-X.; Shi, Y.-N.; Sun, H.; Kelly, P.M. Surface alloying of Mg alloys after surface nanocrystallization. *J. Nanosci. Nanotechnol.* **2008**, *8*, 2724–2728. [CrossRef]
10. Sun, H.; Shi, Y.; Zhang, M.-X.; Lu, K. Surface alloying of an Mg alloy subjected to surface mechanical attrition treatment. *Surf. Coat. Technol.* **2008**, *202*, 3947–3953. [CrossRef]
11. Rokni, M.; Widener, C.; Champagne, V.; Crawford, G. Microstructure and mechanical properties of cold sprayed 7075 deposition during non-isothermal annealing. *Surf. Coat. Technol.* **2015**, *276*, 305–315. [CrossRef]
12. Rokni, M.; Widener, C.; Crawford, G.; West, M. An investigation into microstructure and mechanical properties of cold sprayed 7075 Al deposition. *Mater. Sci. Eng. A* **2015**, *625*, 19–27. [CrossRef]
13. Agar, O.; Alex, A.; Kubacki, G.; Zhu, N.; Brewer, L. Corrosion Behavior of Cold Sprayed Aluminum Alloys 2024 and 7075 in an Immersed Seawater Environment. *Corrosion* **2021**, *77*, 1354–1364. [CrossRef]
14. Bi, J.K.; Loke, Z.C.K.; Lim, C.K.R.; Teng, K.H.T.; Koh, P.K. Mechanical Properties of Cold Sprayed Aluminium 2024 and 7075 Coatings for Repairs. *Aerospace* **2022**, *9*, 65. [CrossRef]
15. Flanagan, T.J.; Bedard, B.A.; Dongare, A.M.; Brody, H.D.; Nardi, A.; Champagne, V.K.; Aindow, M.; Lee, S.-W. Mechanical properties of supersonic-impacted Al6061 powder particles. *Scr. Mater.* **2019**, *171*, 52–56. [CrossRef]
16. Spencer, K.; Fabijanic, D.M.; Zhang, M.-X. The use of Al–Al_2O_3 cold spray coatings to improve the surface properties of magnesium alloys. *Surf. Coat. Technol.* **2009**, *204*, 336–344. [CrossRef]
17. Omar, N.I.; Yamada, M.; Yasui, T.; Fukumoto, M. Bonding mechanism of cold-sprayed TiO_2 coatings on copper and aluminum substrates. *Coatings* **2021**, *11*, 1349. [CrossRef]
18. Dayani, S.; Shaha, K.S.; Ghelichi, R.; Wang, J.; Jahed, H. The impact of AA7075 cold spray coating on the fatigue life of AZ31B cast alloy. *Surf. Coat. Technol.* **2018**, *337*, 150–158. [CrossRef]
19. Shaha, K.S.; Dayani, S.; Jahed, H. Fatigue life enhancement of cast Mg alloy by surface modification in cold spray process. *MATEC Web Conf.* **2018**, *165*, 03014. [CrossRef]
20. Shaha, S.K.; Dayani, S.B.; Xue, Y.; Pang, X.; Jahed, H. Improving corrosion and corrosion-fatigue resistance of AZ31B cast Mg alloy using combined cold spray and top coatings. *Coatings* **2018**, *8*, 443. [CrossRef]
21. Boruah, D.; Zhang, X. Effect of post-deposition solution treatment and ageing on improving interfacial adhesion strength of cold sprayed Ti6Al4V coatings. *Metals* **2021**, *11*, 2038. [CrossRef]
22. Koivuluoto, H.; Larjo, J.; Marini, D.; Pulci, G.; Marra, F. Cold-sprayed Al6061 coatings: Online spray monitoring and influence of process parameters on coating properties. *Coatings* **2020**, *10*, 348. [CrossRef]
23. Rao, Y.; Wang, Q.; Oka, D.; Ramachandran, C.S. On the PEO treatment of cold sprayed 7075 aluminum alloy and its effects on mechanical, corrosion and dry sliding wear performances thereof. *Surf. Coat. Technol.* **2020**, *383*, 125271. [CrossRef]
24. Wei, Y.-K.; Luo, X.-T.; Li, C.-X.; Li, C.-J. Optimization of In-Situ Shot-Peening-Assisted Cold Spraying Parameters for Full Corrosion Protection of Mg Alloy by Fully Dense Al-Based Alloy Coating. *J. Therm. Spray Technol.* **2017**, *26*, 173–183. [CrossRef]
25. Pebere, N.; Riera, C.; Dabosi, F. Investigation of magnesium corrosion in aerated sodium sulfate solution by electrochemical impedance spectroscopy. *Electrochim. Acta* **1990**, *35*, 555–561. [CrossRef]
26. Mangalarapu, T.B.; Kumar, S.; Manthripragada, R.; Gandham, P.; Koppoju, S. Precipitation Behavior of Cold Sprayed Al6061 Coatings. *Materialia* **2022**, *24*, 101510. [CrossRef]
27. Spencer, K.; Zhang, M.-X. Heat treatment of cold spray coatings to form protective intermetallic layers. *Scr. Mater.* **2009**, *61*, 44–47. [CrossRef]
28. Spencer, K.; Luzin, V.; Zhang, M.-X. Structure and properties of cold spray coatings. *Mater. Sci. Forum.* **2010**, *654–656*, 1880–1883. [CrossRef]
29. Zhang, M.-X.; Huang, H.; Spencer, K.; Shi, Y.-N. Nanomechanics of Mg–Al intermetallic compounds. *Surf. Coat. Technol.* **2010**, *204*, 2118–2122. [CrossRef]
30. Pokhmurska, H.; Wielage, B.; Lampke, T.; Grund, T.; Student, M.; Chervinska, N. Post-treatment of thermal spray coatings on magnesium. *Surf. Coat. Technol.* **2008**, *202*, 4515–4524. [CrossRef]
31. Bu, H.; Yandouzi, M.; Lu, C.; MacDonald, D.; Jodoin, B. Cold spray blended Al+Mg17Al12 coating for corrosion protection of AZ91D magnesium alloy. *Surf. Coat. Technol.* **2012**, *207*, 155–162. [CrossRef]
32. Hassani-Gangaraj, S.M.; Moridi, A.; Guagliano, M. Critical review of corrosion protection by cold spray coatings. *Surf. Eng.* **2015**, *31*, 803–815. [CrossRef]
33. Daroonparvar, M.; Bakhsheshi-Rad, H.R.; Saberi, A.; Razzaghi, M.; Kasar, A.K.; Ramakrishna, S.; Menezes, P.L.; Misra, M.; Ismail, A.F.; Sharif, S.; et al. Surface modification of magnesium alloys using thermal and solid-state cold spray processes: Challenges and latest progresses. *J. Magnes. Alloy.* **2022**, *10*, 2025–2061. [CrossRef]

34. Shaha, K.S.; Jahed, H. An in-situ study of the interface microstructure of solid-state additive deposition of AA7075 on AZ31B substrate. *Appl. Surf. Sci.* **2020**, *508*, 144974. [CrossRef]
35. Shuman, D.J.; Costa, A.L.; Andrade, M.S. Calculating the elastic modulus from nanoindentation and microindentation reload curves. *Mater. Charact.* **2007**, *58*, 380–389. [CrossRef]
36. Shaha, S.K.; Jahed, H. Characterization of nanolayer intermetallics formed in cold sprayed al powder on mg substrate. *Materials* **2019**, *12*, 1317. [CrossRef]
37. Wang, L.; Yang, X.; Robson, J.D.; Sanders, R.E.; Liu, Q. Microstructural evolution of cold-rolled AA7075 sheet during solution treatment. *Materials* **2020**, *13*, 2734. [CrossRef]
38. Bobzin, K.; Wietheger, W.; Hebing, J.; Gerdt, L. Softening Behavior of Cold-Sprayed Aluminum-Based Coatings AA1200 and AA7075 During Annealing. *J. Therm. Spray Technol.* **2021**, *30*, 358–370. [CrossRef]
39. Ghelichi, R.; MacDonald, D.; Bagherifard, S.; Jahed, H.; Guagliano, M.; Jodoin, B. Microstructure and fatigue behavior of cold spray coated Al5052. *Acta Mater.* **2012**, *60*, 6555–6561. [CrossRef]
40. Mercelis, P.; Kruth, J. Residual stresses in selective laser sintering and selective laser melting. *Rapid Prototyp. J.* **2006**, *12*, 254–265. [CrossRef]
41. Villuendas, A.; Jorba, J.; Roca, A. The role of precipitates in the behavior of Young's modulus in aluminum alloys. *Met. Mater. Trans. A* **2014**, *45*, 3857–3865. [CrossRef]